Optimal Shape for Optical Absorption in Organic Thin Film Solar Cells

Songtao Xia[†], Guangyong Li[‡], and Xiaoping Qian[*†]

[†]Department of Mechanical, Materials, University of Wisconsin-Madison, Madison, WI 53706-1572
[‡]Department of Electrical and Computer Engineering, University of Pittsburgh, Pittsburgh, PA 15261

Abstract

The power conversion efficiency of organic solar cells can be increased by using light trapping geometries, which enhance the light absorption. In this paper, we analyze the optical performance of organic thin film solar cells using the finite element method solving the Maxwell equations. Shape optimization is then performed with the goal of maximizing the light absorption in the active layer, while keeping its thickness low. The optimization algorithm is based on the gradient of the objective function, where sensitivity is obtained from the adjoint approach. To avoid irregular shapes in the optimized structures, two different shape representation techniques, finite element node based curve representation in conjunction with the Helmholtz filter and B-spline curve representation with varying number of control points are used. Both are demonstrated being effective in smoothing the design shapes. Periodic grating structures are observed in the optimized shapes and significant increase in light absorption is achieved in the active layer with low thickness.

1   Introduction

Organic thin film solar cells are attractive because they can be fabricated as large area devices at low cost and at relatively low processing temperatures, compared with inorganic solar cells [1]. However, one of the main drawbacks preventing it from commercialization is the insufficient light absorption in the thin films [2, 3, 4]. The

---

[*]All correspondence should be addressed to qian@engr.wisc.edu.

low mobility of charge carriers in organic materials requires a low thickness of the active layer to reduce the probability of charge recombination [5, 6]. On the other hand, with such a limited thickness the optical property of the materials makes it difficult to harvest sufficient energy from sunlight. Therefore to achieve desirable device efficiency light trapping approaches are desired. Since the light absorption is greatly dependent on the specific geometry of the device, structural geometry improvements are becoming a vital part of the research. However, a recent review [7] reported that very few works have been done to fully optimize the structure of OSCs [8, 3, 9, 10]. In [3] Raman et al numerically demonstrated that 1D periodic, 2D circular and multi-level gratings lying on top of OSC stack can enhance light absorption. In [9] Nalwa et al analyzed the design of organic photovoltaic cells using the finite element method simulations. The energy dissipation in the active layer is studied as a function of active layer thickness, pitch and height of the underlying textures. Tvingstedt et al in [10] studied the light absorption of V-shape OSCs with various folding angles. All these works were based on some simple a priori shapes, such as rectangular, circular and V-shape, with simple modification of shape sizes. Yu et al in [8] presented a general approach to achieve highly-efficient designs of slot-waveguide based cell using topology optimization. However, in their simulated model, the thickness of active layer is fixed at 10 nm. Thus what is the true optimal shape for maximal optical absorption remains unclear.

Shape optimization provides an alternative to help understand the effect of geometrical changes in the light absorption of OSCs. The optimization problem can be formulated with the objective of maximizing light absorption in the active layer under the constraint of Maxwell equations, which governs the light propagation in the device. To ensure quick convergence, we adopt a gradient based optimization approach where analytical sensitivity is required for the optimization algorithm. This is obtained efficiently by solving an adjoint system associated with the original state system.

However, with such formulation the existence of solution to the shape optimization problem is not guaranteed. This has been studied extensively by many researchers. One of the means to provide existence of solutions is using regularity assumptions for the boundary of the unknown domains [11, 12, 13]. Motivated by these work, in our work we use filter technique to regularize the design boundary. A filter by solving a Helmholtz equation has been used in shape and topology optimization [14, 15, 16]. We also introduce another filter technique, the B-spline. It leads to smooth shape with relatively a small number of control points capable of representing a large class of curves and is also compatible with widely used shape representations in common CAD systems. Such advantages make it an attractive

alternative to represent the boundaries in shape optimization [17, 18].

Another concern in designing novel structures of OSCs is their manufacturability. Much progress has been made recently on the fabrication of nano-scaled structures using polymer materials. Zhu et al presented an approach to fabricate the grating strengthened polymer solar cell with optical enhancement [19]. They used an improved soft lithographic approach using capillary force molding (CFM), which is a simple method of fabricating nanometer scale patterns with low cost and high resolution [20]. Nalwa et al demonstrated that it was possible to realize conformal active-layers on light-trapping textured substrates, and thus higher efficiency solar cells, if the topographical dimensions of textured substrates were carefully chosen [21]. They successfully fabricated a device of textured substrate using laser interference lithography. Na et al applied periodic submicrometer gratings to a bulk heterojunction cell to enhance the light absorption and increased the efficiency [22]. The triangular shaped structure is produced via a damage-free soft lithographic approach using photoresponsive azo polymers and PDMS as masters and as stamps, respectively. The development of such new fabrication methods thus opens the door for designing optimal OSCs shapes for maximal optical absorption.

The remaining of the paper is organized as follows. Section 2 describes the optical modeling of OSCs and Section 3 gives the formulation of the optimization problem, followed by the sensitivity analysis in Section 4. In Section 5, the shape smoothing techniques are introduced. The implementation of our approach is shown in Section 6 and finally some conclusions are drawn in Section 7.

2   Optical modeling

A frequently used parameter to characterize the performance of OSCs responding to incident light is the external quantum efficiency, which is defined as the ratio of the number of collected charge carriers to the number of incident photons. Based on the energy flow in OSCs [7], the external quantum efficiency can be divided into two parts, the light absorption efficiency and the internal quantum efficiency. While the internal quantum efficiency has reached close to 100%, as recently reported in [23], the light absorption efficiency (as fraction of incident power) remains $20\% - 50\%$ for planar OSCs depending on the active layer thickness [9, 24]. Therefore the overall performance of OSCs would be significantly improved if the light absorption efficiency can be increased. Optical modeling has been proved to be an effective approach to understand the physics of OSCs and calculate the light absorption.

Since the geometry of the layers would change and could be of any freeform shape during optimization, the commonly used optical transfer matrix method for planar

solar cells would no longer be suitable here. Therefore in this paper we adopt a finite element based approach to solve the Maxwell equations which govern the light propagation in the device.

2.1 State equation and boundary conditions

The Maxwell equations give a full description of the electromagnetic field within the layered structure, including interference, diffraction, and polarization effects of the light. Here we limit our discussion to materials that are linear and isotropic, then the Maxwell equations for light propagation in such materials can be expressed as [25],

$$\nabla \cdot E = 0, \tag{1a}$$

$$\nabla \cdot B = 0, \tag{1b}$$

$$\nabla \times E = -\frac{\partial B}{\partial t}, \tag{1c}$$

$$\nabla \times B = \epsilon\mu\frac{\partial E}{\partial t}, \tag{1d}$$

where E and B are the electric and magnetic field respectively, ϵ is the dielectric constant (or the permittivity), and μ is the magnetic permeability. Taking the curl of Eq. (1c) and substituting into Eq. (1d) gives

$$\nabla \times \nabla \times E = -\epsilon\mu\frac{\partial^2 E}{\partial t^2}. \tag{2}$$

With the use of Eq. (1a), Eq. (2) can be rewritten in terms of the Laplacian operation,

$$\nabla^2 E - \epsilon\mu\frac{\partial^2 E}{\partial t^2} = 0. \tag{3}$$

It is straight forward to check that the general solution of Eq. (3) is plane wave in the form of (assume the light is propagating along x-direction)

$$E(\boldsymbol{x}, t) = Ae^{i(\pm\tilde{k}\boldsymbol{x}+\omega t)}, \tag{4}$$

where ω is the angular frequency of the travelling light, $\tilde{k} = \omega\sqrt{\epsilon\mu}$ is the wave number and A is a constant. To obtain the particular solution, several appropriate boundary conditions need to be applied. On the incident boundary Γ_{in}, the planar wave can be viewed as a superposition of incident and reflected wave and written as

$$E(\boldsymbol{x}, t) = E_0 e^{i(\tilde{k}\boldsymbol{x}\cdot\boldsymbol{s}+\omega t)} + Re^{i(-\tilde{k}\boldsymbol{x}\cdot\boldsymbol{s}+\omega t)}, \tag{5}$$

4

where $\boldsymbol{s}$ is the normal to the boundary pointing outward, E_0 and R are the electric field amplitudes of incident and reflected wave respectively. Differentiating Eq. (5) with respect to t and $\boldsymbol{s}$ respectively gives

$$\frac{\partial E}{\partial t} = E_0 i\omega e^{i(\tilde{k}\boldsymbol{x}\cdot\boldsymbol{s}+\omega t)} + Ri\omega e^{i(-\tilde{k}\boldsymbol{x}\cdot\boldsymbol{s}+\omega t)}, \tag{6}$$

$$\frac{\partial E}{\partial \boldsymbol{s}} = E_0 i\tilde{k} e^{i(\tilde{k}\boldsymbol{x}\cdot\boldsymbol{s}+\omega t)} - Ri\tilde{k} e^{i(-\tilde{k}\boldsymbol{x}\cdot\boldsymbol{s}+\omega t)}. \tag{7}$$

Adding Eq. (6) and (7) we obtain

$$\frac{\partial E}{\partial t} + \frac{\omega}{\tilde{k}}\frac{\partial E}{\partial \boldsymbol{s}} = 2i\omega E_0 e^{i(\tilde{k}\boldsymbol{x}\cdot\boldsymbol{s}+\omega t)}. \tag{8}$$

At the bottom of the device Γ_{out} where light propagates out of the structure, a first order absorbing boundary condition is assumed, meaning the outgoing light will be totally absorbed by the ambient environment and no reflection will be caused. This truncates the infinite open domain to a finite computational domain [25],

$$\frac{\partial E}{\partial t} + \frac{\omega}{\tilde{k}}\frac{\partial E}{\partial \boldsymbol{s}} = 0. \tag{9}$$

On the two sides Γ_{side} we assume zero flux which is

$$\frac{\partial E}{\partial \boldsymbol{s}} = 0. \tag{10}$$

For the conditions across the interfaces of different layers, the total electric field is required to be continuous across the two sides of the interface, which is automatically satisfied by solving the Maxwell equation over the whole domain [25]. Now if we substitute the general solution

$$E(\boldsymbol{x}, t) = E(\boldsymbol{x})e^{i\omega t}, \tag{11}$$

where $E(\boldsymbol{x})$ is the complex electric amplitude of the incident wave, into Eqs. (3), (8) and (9), we obtain the following time harmonic Helmholtz equation system,

$$\nabla^2 E + \tilde{k}^2 E = 0, \qquad\qquad \text{in } \Omega \tag{12a}$$

$$\frac{\partial E}{\partial \boldsymbol{s}} + i\tilde{k}E = 2i\tilde{k}E_0, \qquad\qquad \text{on } \Gamma_{in} \tag{12b}$$

$$\frac{\partial E}{\partial \boldsymbol{s}} + i\tilde{k}E = 0, \qquad\qquad \text{on } \Gamma_{out} \tag{12c}$$

$$\frac{\partial E}{\partial \boldsymbol{s}} = 0, \qquad\qquad \text{on } \Gamma_{side} \tag{12d}$$

where $\tilde{k} = 2\pi\tilde{n}/\lambda$, and λ is the wavelength of the light, $\tilde{n} = \kappa + i\eta$ is the complex refractive index of the materials with κ and η being the real and imaginary part respectively. For each material, the values of κ and η vary with the incident light and can be viewed as continuous functions of the wavelength λ of the incident light. In the derivation of above equation, we have also made use of some frequently used relation in wave propagation, i.e. $\tilde{n}^2 = \epsilon\mu, \omega = 2\pi f = 2\pi c/\lambda$. Thanks to the well-known Sommerfeld radiation condition [26], the existence and uniqueness of Eq. (12) in homogeneous media have been well developed. In the case of smooth domains, [27] also gives a very complete description of the use of layer potentials for boundary value problems for the Helmholtz equation on smooth domains.

2.2 Energy dissipation

Based on the Poynting theorem of energy conservation for the electromagnetic field, the time averaged energy flow dissipation per unit volume for monochromatic incident light at the point $\boldsymbol{x}$ is

$$Q(\lambda, \boldsymbol{x}) = 2\pi c\epsilon_0 \frac{\kappa\eta}{\lambda}|E(\boldsymbol{x})|^2, \tag{13}$$

where c is the speed of light and ϵ_0 is the permittivity of vacuum. This equation shows that, for monochromatic incident light, the energy absorbed at position $\boldsymbol{x}$ in the structure is proportional to the squared modulus of the electric field $|E(\boldsymbol{x})|^2$, which is obtained by solving Eq. (12).

3 Formulation of the optimization problem

Due to its promising performance, the bulk heterojunction OSCs where the active layer is a blend of donor and acceptor materials, have been gaining a lot of attention [2]. In a typical bulk heterojunction OSC, the domain Ω consists of several layers of different materials and the shape can be changed. However, only the light absorbed in the active layer contributes to the final output power. Therefore our interest is to find the optimal shape which maximizes the energy absorption in the active layer, under the assumption that all layers have the same shape, as shown in Fig. 1. The simulated OSC model consists of five layers: Air, ITO, PEDOT:PSS, P3HT:PCBM and Al respectively from top to bottom. Γ_{in} and Γ_{out} are the boundaries where light incidents on and propagates out respectively, Γ_{side} are the boundaries on the two sides, Γ_d is the design shape to be determined. The shadowed domain Ω^A is the active layer in which the light absorption is of interest.
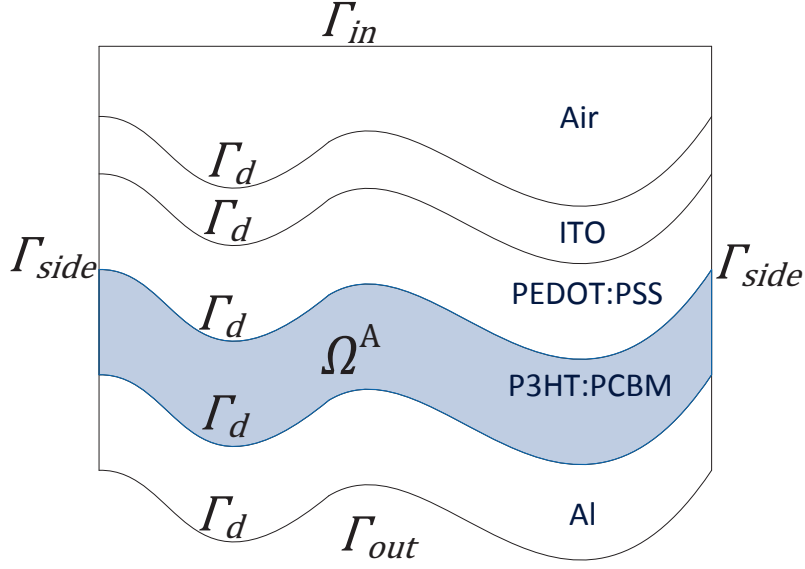
Figure 1: Schematic illustration of simulated OSC structure.

3.1 Objective function

For single frequency incident light, the total energy absorbed in the active layer can be calculated by integrating Eq. (13) over the domain of active layer. To cast it as a standard minimization problem, we define the objective function as,

$$\mathcal{F}_\lambda = -\int_{\Omega^A} Q(\lambda, \boldsymbol{x}) = -2\pi c\varepsilon_0 \frac{\kappa\eta}{\lambda} \int_{\Omega^A} |E|^2 d\Omega, \tag{14}$$

where Ω^A represents the domain of active layer as shown in Fig. 1. In practice the incident light usually includes a wide range of frequencies, such as the sunlight. Then the total energy absorbed will be a sum of Eq. (14) and the objective function will be the following,

$$\mathcal{F}_{sum} = -\sum_{\lambda=\underline{\lambda}}^{\overline{\lambda}} \mathcal{F}_\lambda, \tag{15}$$

where $\underline{\lambda}$ and $\overline{\lambda}$ are the lower and upper limit respectively of the incident light wavelength corresponding to the absorption spectrum of the material.

7

3.2 Shape parameterization

Eqs. (14) and (15) show that the value of the objective function depends on the area of the active layer and the electric field distribution E. Since increasing the area is trivial and not of our interest here, we focus on the electric field distribution, which depends on the structure of OSCs, that is, the shape of the layer boundaries. To make it simple, we seek a structure where all layers are conformal, i.e. all layers have the same shape. For this purpose all the interior layer shapes are represented by the same curve throughout the optimization and is denoted as Γ_d. As shown in Fig. 2, two different methods are used to represent the design shapes.
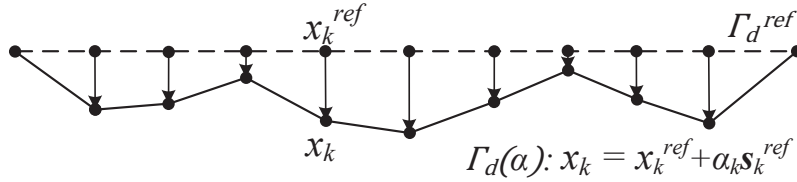
(a) Finite element node based shape representation. The black dots are the nodes and the arrows indicate the movement of the nodes.
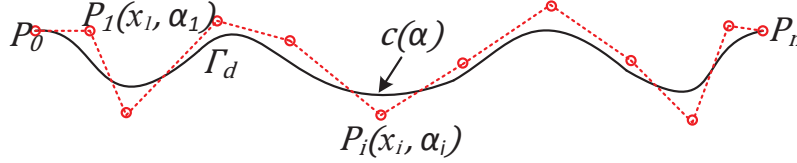
(b) B-spline based shape representation. The red circles are the control points.

Figure 2: Representations of design shapes.

For the first shape representation, the design shape Γ_d is represented based on the finite element nodes. After discretization, the position of the kth node $\boldsymbol{x}_k$ on the design shape is defined as

$$\boldsymbol{x}_k = \boldsymbol{x}_k^{ref} + \alpha_k \boldsymbol{s}_k^{ref}, \tag{16}$$

where $\boldsymbol{x}_k^{ref}$ is the corresponding mesh node on the reference shape Γ_d^{ref} which is a straight line, $\boldsymbol{s}_k^{ref}$ is the unit normal of the node and α_k is the movement and is used as the design variable. Here, to simplify the problem the nodes are only allowed to move in the y direction. In this way, the number of design variables will depend on the discretization of the domain.

The second shape representation is based on B-splines, a commonly used geometry representation in computer aided design (CAD) systems. With a number of

control points $\boldsymbol{P}_i,\ i = 0, \cdots, n$, a $d-$th degree B-spline is defined as

$$\boldsymbol{c}(\boldsymbol{\alpha}) = B(u, \boldsymbol{\alpha}) = \sum_{i=0}^{m} P_i(\boldsymbol{\alpha}) N_{i,d}(u), \quad u \in [u_{d-1}, u_{m+1}] \tag{17}$$

where $\boldsymbol{\alpha}$ are the design variables which determine the coordinates of the control points $\boldsymbol{P}_i$ (Fig. 2(b)), and $N_{i,d}$ are the basis functions defined as

$$N_{i,0}(u) = \begin{cases} 1 & \text{if } u_i \le u \le u_{i+1}, \\ 0 & \text{otherwise.} \end{cases} \tag{18}$$

$$N_{i,d}(u) = \frac{u - u_i}{u_{i+d} - u_i} N_{i,d-1}(u) + \frac{u_{i+d+1} - u}{u_{i+d+1} - u_{i+1}} N_{i+1,d-1}(u). \tag{19}$$

Here $u_i,\ i = 0, \cdots, m$ are the knots of the B-spline. In this work, the cubic B-spline is used and again the $x-$ coordinates of the control points are given, that is, the control points are only allowed to move in the $y-$ direction. Particularly we will discuss later that, by choosing different number of control points we can reduce the oscillation that usually occur in shape optimization.

Now we can formulate the optimization problem as

$$\begin{cases} \min_{\boldsymbol{\alpha}} & \mathcal{F}_\lambda = -2\pi c \varepsilon_0 \frac{\kappa \eta}{\lambda} \int_{\Omega^A} |E|^2 d\Omega, \text{ for incident light of single frequency , or} \\ & \mathcal{F}_{sum} = -2\pi c \varepsilon_0 \sum_{\lambda=\underline{\lambda}}^{\overline{\lambda}} \left(\frac{\kappa \eta}{\lambda} \int_{\Omega^A} |E|^2 d\Omega \right), \text{ for incident light of multi-frequency.} \\ \text{s.t.} & \mathcal{D}(E(\boldsymbol{\alpha}), \boldsymbol{\alpha}) = 0 \\ & \boldsymbol{\alpha}_{\min} \le \boldsymbol{\alpha} \le \boldsymbol{\alpha}_{\max} \end{cases} \tag{20}$$

where $\mathcal{D}(E(\boldsymbol{\alpha}), \boldsymbol{\alpha}) = 0$ is the state equation (12) and $\boldsymbol{\alpha}_{\min} \le \boldsymbol{\alpha} \le \boldsymbol{\alpha}_{\max}$ is the box constraint controlling the thickness of each layer.

Directly solving this problem may not be successful since the existence of solution is not guaranteed. Motivated by the work of [11, 12, 13], in this work we use filter technique to regularize the design boundary and provide the existence of solution, as will be discussed in Section 5. A detailed proof of existence of solution for such elliptic boundary-value problem can also be found in [11, 12, 13, 28].

4 Sensitivity analysis

The gradient based optimization approach is used to solve the optimization problem. Specifically, the well-established method of moving asymptotes (MMA) is used.

9

More details about this method can be found in [29]. MMA uses a special type of convex approximation. For each step of the iterative process, a strictly convex approximating subproblem is generated and solved. The generation of these sub-problems is controlled by the so-called moving asymptotes, which both stabilize and speed up the convergence of the general process. It requires the sensitivity of the objective function and constraints with respect to the design variables. To solve the problem efficiently the exact sensitivity must be obtained in an efficient way. Here we follow the first-discretize-then-optimize scheme, where the state equation and objective function are discretized first and based on the discretized system the sensitivity is derived. In the following we describe how the Lagrangian approach [13] can be used to obtain the analytical sensitivity.

4.1 Discretization of state equation and objective function

For the derivation of the gradient, it is convenient to work with the state equation (12) in variational form:

Find $E \in H^1(\Omega)$ such that

$$
\begin{aligned}
&\int_\Omega \nabla \overline{v} \cdot \nabla E d\Omega - \tilde{k}^2 \int_\Omega \overline{v} E d\Omega + i\tilde{k} \int_{\Gamma_{in} \cup \Gamma_{out}} \overline{v} E d\Gamma \\
&= 2i\tilde{k} E_0 \int_{\Gamma_{in}} \overline{v} d\Gamma, \qquad \forall v \in H^1(\Omega),
\end{aligned}
\tag{21}
$$

where $H^1(\Omega)$ is the space of complex-valued functions in which the functions as well as their gradients are square-integrable. v is the test function and an overbar denotes complex conjugate.

After discretization, the domain Ω is approximated by Ω^h, the union of the discretized finite elements. On Ω^h, the solution to the state problem E is approximated in the finite-dimensional space V^h of continuous, complex-valued functions. We have

$$
V^h = \mathrm{span}\{w_j\}_{j=1}^N \subset H^1(\Omega^h),
$$

where w_j are standard nodal basis functions, N is the total number of node points, and $H^1(\Omega^h)$ is the space of complex-valued functions on Ω^h such that the function itself and first order derivatives are square-integrable. The finite element approximation to the solution E of state equation (12) is denoted E^h. which is expressed as a linear combination of the basis functions w_j,

$$
E^h(\boldsymbol{x}) = \sum_{j=1}^N E_j w_j(\boldsymbol{x}), \quad E_j \in \mathbb{C}
\tag{22}
$$

10

where $\mathbb{C}$ is the space of complex values. And E^h is the solution to equation

$$\int_{\Omega^h} \nabla w_j \cdot \nabla E^h d\Omega - \tilde{k}^2 \int_{\Omega^h} w_j E^h d\Omega + i\tilde{k} \int_{\Gamma_{in} \cup \Gamma_{out}} w_j E^h d\Gamma$$
$$= 2i\tilde{k}E_0 \int_{\Gamma_{in}} w_j d\Gamma \text{ for } j = 1, \cdots, N. \tag{23}$$

Objective function (14) is discretized by substituting E with E^h, and written as function of E^h and the discretized domain of active layer $\Omega^{h,A}$,

$$\mathcal{F}^h(E^h, \Omega^{h,A}) = -\int_{\Omega^{h,A}} Q(\boldsymbol{x}) = -2\pi c \varepsilon_0 \frac{\kappa\eta}{\lambda} \int_{\Omega^{h,A}} |E^h|^2 d\Omega = -2\pi c \varepsilon_0 \frac{\kappa\eta}{\lambda} \int_{\Omega^{h,A}} \overline{E^h} E^h d\Omega. \tag{24}$$

Now we have the discrete optimization problem as

$$\begin{cases} \min_{\boldsymbol{\alpha}} \quad \mathcal{F}^h_\lambda = -2\pi c \varepsilon_0 \frac{\kappa\eta}{\lambda} \int_{\Omega^{h,A}} \overline{E^h} E^h d\Omega, \text{ for incident light of single frequency , or} \\ \\ \quad\quad \mathcal{F}^h_{sum} = -2\pi c \varepsilon_0 \sum_{\lambda=\underline{\lambda}}^{\overline{\lambda}} \left(\frac{\kappa\eta}{\lambda} \int_{\Omega^{h,A}} \overline{E^h} E^h d\Omega \right), \text{ for incident light of multi-frequency.} \\ \\ \text{s.t.} \quad \mathcal{D}^h(E^h(\boldsymbol{\alpha}), \boldsymbol{\alpha}) = 0 \\ \\ \quad\quad \boldsymbol{\alpha}_{\min} \leq \boldsymbol{\alpha} \leq \boldsymbol{\alpha}_{\max} \end{cases} \tag{25}$$

where $\mathcal{D}^h(E^h(\boldsymbol{\alpha}), \boldsymbol{\alpha}) = 0$ is the discretized state equation (23) and $\boldsymbol{\alpha}_{\min} \leq \boldsymbol{\alpha} \leq \boldsymbol{\alpha}_{\max}$ is the box constraint controlling the thickness of each layer.

To simplify the notation, the superscript h will be suppressed from functions in V^h in the following sections.

4.2 The adjoint method

The adjoint method begins with adjoining the constraint, in this case the weak form of the state equation, to the objective function via a Lagrange multiplier $\overline{U}$ (The complex conjugate value is used for convenience in later derivation) [30]. The Lagrangian functional $\mathcal{L}$ is then defined as

$$\mathcal{L}(\boldsymbol{x}, E, \overline{U}) = \mathcal{F}(\boldsymbol{x}, E) + \overline{U}\mathcal{G}(\boldsymbol{x}, E), \tag{26}$$

where $\mathcal{G}(\boldsymbol{x}, E) = 0$ represents the state equation in the weak form Eq. (23). Note that the Lagrangian functional is essentially the objective function when the state equation is satisfied. Since the positions of mesh nodes are directly related to the

11

design variables controlling the design boundary, we wish to find the gradient of the Lagrangian with respect to the position of the mesh nodes, i.e. $\dfrac{\partial \mathcal{L}}{\partial \boldsymbol{x_k}}$.

The first variation of the Lagrangian functional is given by

$$\delta \mathcal{L} = (\frac{\partial \mathcal{F}}{\partial E} + \overline{U}\frac{\partial \mathcal{G}}{\partial E})\delta E + \sum_{k=1}^{N}(\frac{\partial \mathcal{F}}{\partial \boldsymbol{x}_k} + \overline{U}\frac{\partial \mathcal{G}}{\partial \boldsymbol{x}_k})\delta \boldsymbol{x}_k + \mathcal{G}\delta \overline{U}, \quad (27)$$

where $\boldsymbol{x}_k$ are the mesh nodes. It is easy to see that the last term vanishes since the state equation is satisfied in each iteration. Since we are only interested in the relation between $\delta \mathcal{L}$ and $\delta \boldsymbol{x}_k$, it is natural to eliminate the first term involving the variation of the state variable by setting

$$(\frac{\partial \mathcal{F}}{\partial E} + \overline{U}\frac{\partial \mathcal{G}}{\partial E})\delta E = 0, \quad (28)$$

or, in the variational form

$$\delta \mathcal{F}(\delta E) + \overline{U}\delta \mathcal{G}(\delta E) = 0, \quad (29)$$

which is known as the adjoint equation and can be solved to obtain U. The notation $\delta \mathcal{F}(\delta E)$ denotes a real number, the action of $\delta \mathcal{F}$ on its argument δE. From the objective function (24) we can get

$$\delta \mathcal{F}(\delta E) = -2\pi c\varepsilon_0 \frac{\kappa\eta}{\lambda}\int_{\Omega^A}(\overline{\delta E}E + \overline{E}\delta E)d\Omega = -4\pi c\varepsilon_0\frac{\kappa\eta}{\lambda}\Re\left(\int_{\Omega^A}\overline{E}\delta E d\Omega\right), \quad (30)$$

where $\Re$ means the real part of the complex value. While U is arbitrary, now we pick $U \subset V^h$ which can be expanded as

$$U(\boldsymbol{x}) = \sum_{j=1}^{N}U_j w_j(\boldsymbol{x}), \quad U_j \in \mathbb{C}. \quad (31)$$

Multiplying it with the weak form of state equation (23) and summing over all $j \in \{1, 2, \cdots, N\}$, the second term in Eq. (29) can be written as following

$$\overline{U}\delta \mathcal{G}(\delta E) = \int_{\Omega}\nabla \overline{U}\cdot \nabla \delta E d\Omega - \tilde{k}^2\int_{\Omega}\overline{U}\delta E d\Omega + i\tilde{k}\int_{\Gamma_{in}\cup\Gamma_{out}}\overline{U}\delta E d\Gamma. \quad (32)$$

Substituting Eq. (30) and Eq. (32) into Eq. (29), and taking its complex conjugate, noting that the real part of the function is what we are interested in and equals zero, we obtain

$$\int_{\Omega}\nabla U\cdot \nabla\overline{\delta E}d\Omega - \overline{\tilde{k}}^2\int_{\Omega}U\overline{\delta E}d\Omega - i\overline{\tilde{k}}\int_{\Gamma_{in}\cup\Gamma_{out}}U\overline{\delta E}d\Gamma = 4\pi c\varepsilon_0\frac{\kappa\eta}{\lambda}\int_{\Omega^A}\overline{\delta E}E d\Omega \quad (33)$$

This is the weak form of the adjoint equation where $\overline{\delta E}$ is the test function of U.

4.3 Sensitivity with respect to the variation of mesh nodes

With the state equation and adjoint equation, the nonzero terms remaining in the variation of the Lagrangian functional (27) is

$$\delta\mathcal{L} = \sum_{k=1}^{N} \delta\mathcal{L}(\delta\boldsymbol{x}_k) = \sum_{k=1}^{N} \frac{\partial\mathcal{L}}{\partial\boldsymbol{x}_k}\delta\boldsymbol{x}_k = \sum_{k=1}^{N}(\frac{\partial\mathcal{F}}{\partial\boldsymbol{x}_k} + \overline{U}\frac{\partial\mathcal{G}}{\partial\boldsymbol{x}_k})\delta\boldsymbol{x}_k, \tag{34}$$

or in the variational form

$$\frac{\partial\mathcal{L}}{\partial\boldsymbol{x}_k} \cdot \delta\boldsymbol{x}_k = \delta\mathcal{F}(\delta\boldsymbol{x}_k) + \overline{U}\delta\mathcal{G}(\delta\boldsymbol{x}_k), \tag{35}$$

where the variations with respect to the mesh nodes need to be determined explicitly, i.e. written in terms of the state and adjoint variables E and U only. Before we proceed, several fundamental formulas used in the derivations need to be stated.

Lemma 1. *Let w_k and w_j be any two of the finite element basis functions, if the position of a mesh node $\boldsymbol{x}_k$ is varied by $\delta\boldsymbol{x}_k$, we have the following relation for the variation of the basis function [12]*

$$\delta w_j(\boldsymbol{x}, \delta\boldsymbol{x}_k) = -w_k\delta\boldsymbol{x}_k \cdot \nabla w_j.$$

Lemma 2. *Let K represents the set of all mesh nodes of the domain, if the position of a mesh node $k \in K$ is varied by $\delta\boldsymbol{x}_k$, we have [12]*

$$\delta\left(\int_{T_e} g d\Omega\right) = \int_{T_e} \delta g d\Omega + \delta\boldsymbol{x}_k \cdot \int_{T_e} \nabla(g w_k)d\Omega,$$

where T_e is any element in the mesh, and g is a smooth function defined in T_e.

Lemma 1 is obtained by direct differentiating the finite element basis function $w_j(\boldsymbol{x}_k) = \delta_{jk}$ for Lagrange elements. Lemma 2 can be derived using the mean value theorem and the divergence theorem. For details about the proofs please see [12].

Using Lemma 2 when differentiating the discrete objective function (24) with respect to a variation $\delta\boldsymbol{x}_k$ of mesh node k, we obtain

$$\delta\mathcal{F}(\delta\boldsymbol{x}_k) = -2\pi c\varepsilon_0\frac{\kappa\eta}{\lambda}\Re\left\{2\int_{\Omega^A} \overline{\delta E}E d\Omega + \delta\boldsymbol{x}_k \cdot \int_{\Omega^A} \nabla(w_k\overline{E}E)d\Omega\right\}. \tag{36}$$

Similarly differentiating both sides of Eq. (22) with respect to a variation $\delta \boldsymbol{x}_k$ of mesh node k and using Lemma 1 gives

$$
\begin{aligned}
\delta E &= \sum_{j=1}^{N} \delta E_j w_j + \sum_{j=1}^{N} E_j \delta w_j \\
&= \sum_{j=1}^{N} \delta E_j w_j - \sum_{j=1}^{N} w_k \delta \boldsymbol{x}_k \cdot \nabla(E_j w_j) \\
&= \widehat{\delta E} - w_k \delta \boldsymbol{x}_k \cdot \nabla E,
\end{aligned}
\tag{37}
$$

where

$$
\widehat{\delta E} = \sum_{j=1}^{N} \delta E_j w_j.
\tag{38}
$$

Combining Eq. (36) and Eq. (37) yields

$$
\begin{aligned}
& \delta \mathcal{F}(\delta \boldsymbol{x}_k) \\
&= -2\pi c \varepsilon_0 \frac{\kappa \eta}{\lambda} \Re \left\{ 2 \int_{\Omega^A} \overline{\widehat{\delta E}} E d\Omega - 2\delta \boldsymbol{x}_k \cdot \int_{\Omega^A} w_k E \, \nabla \overline{E} d\Omega + \delta \boldsymbol{x}_k \cdot \int_{\Omega^A} \nabla(w_k \overline{E} E) d\Omega \right\}
\end{aligned}
\tag{39}
$$

The term $\overline{U} \delta \mathcal{G}(\delta \boldsymbol{x}_k)$ is computed by writing the integrals as sums over all M elements as the following,

$$
\begin{aligned}
& \overline{U} \delta \mathcal{G}(\delta \boldsymbol{x}_k) \\
&= \sum_{e=1}^{M} \left\{ \int_{T_e} \nabla \delta \overline{U} \cdot \nabla E d\Omega + \int_{T_e} \nabla \overline{U} \cdot \nabla \delta E d\Omega + \delta \boldsymbol{x}_k \cdot \int_{T_e} \nabla(w_k \nabla \overline{U} \cdot \nabla E) d\Omega \right. \\
& \left. - \tilde{k}^2 \int_{T_e} \delta \overline{U} E d\Omega - \tilde{k}^2 \int_{T_e} \overline{U} \delta E d\Omega - \tilde{k}^2 \delta \boldsymbol{x}_k \cdot \int_{T_e} \nabla(w_k \overline{U} E) d\Omega \right\} \\
& + i\tilde{k} \int_{\Gamma_{in} \cup \Gamma_{out}} \delta \overline{U} E d\Gamma + i\tilde{k} \int_{\Gamma_{in} \cup \Gamma_{out}} \overline{U} \delta E d\Gamma + i\tilde{k} \delta \boldsymbol{x}_k \cdot \int_{\Gamma_{in} \cup \Gamma_{out}} \nabla(w_k \overline{U} E) d\Gamma.
\end{aligned}
\tag{40}
$$

We should notice that the boundary integrals on Γ_{in} can be eliminated since the incident boundary is fixed.

After some manipulation using the two lemmas and Eq. (37), taking the complex

14

conjugate of Eq. (40) and summing up the integrals, we obtain

$$
\begin{aligned}
&\overline{U}\delta\mathcal{G}(\delta\boldsymbol{x}_k)\\
=&\int_{\Omega}\nabla U\cdot\nabla\overline{\widehat{\delta E}}d\Omega-\overline{\widehat{k}}^2\int_{\Omega}U\overline{\widehat{\delta E}}d\Omega-i\overline{\widehat{k}}\int_{\Gamma_{in}\cup\Gamma_{out}}U\overline{\widehat{\delta E}}d\Gamma-\delta\boldsymbol{x}_k\cdot\int_{\Omega}\nabla U\nabla w_k\cdot\nabla\overline{E}d\Omega\\
&-\delta\boldsymbol{x}_k\cdot\int_{\Omega}\nabla\overline{E}\nabla U\cdot\nabla w_k d\Omega+\delta\boldsymbol{x}_k\cdot\int_{\Omega}\nabla w_k\nabla U\cdot\nabla\overline{E}d\Omega\\
&-\overline{\widehat{k}}^2\delta\boldsymbol{x}_k\cdot\int_{\Omega}U\overline{E}\nabla w_k d\Omega-i\overline{\widehat{k}}\delta\boldsymbol{x}_k\cdot\int_{\Gamma_{out}}U\overline{E}\nabla w_k d\Gamma.
\end{aligned}
\tag{41}
$$

Adding Eq. (39) and Eq. (41) together and reordering the terms gives us

$$
\begin{aligned}
&\delta\mathcal{F}(\delta\boldsymbol{x}_k)+\overline{U}\delta\mathcal{G}(\delta\boldsymbol{x}_k)\\
=&\Re\left\{-4\pi c\varepsilon_0\frac{\kappa\eta}{\lambda}\int_{\Omega^A}\overline{\widehat{\delta E}}Ed\Omega+\int_{\Omega}\nabla U\cdot\nabla\overline{\widehat{\delta E}}d\Omega-\overline{\widehat{k}}^2\int_{\Omega}U\overline{\widehat{\delta E}}d\Omega-i\overline{\widehat{k}}\int_{\Gamma_{in}\cup\Gamma_{out}}U\overline{\widehat{\delta E}}d\Gamma\right.\\
&-\delta\boldsymbol{x}_k\cdot\int_{\Omega}\nabla U\nabla w_k\cdot\nabla\overline{E}d\Omega-\delta\boldsymbol{x}_k\cdot\int_{\Omega}\nabla\overline{E}\nabla U\cdot\nabla w_k d\Omega\\
&+\delta\boldsymbol{x}_k\cdot\int_{\Omega}\nabla w_k\nabla U\cdot\nabla\overline{E}d\Omega-\overline{\widehat{k}}^2\delta\boldsymbol{x}_k\cdot\int_{\Omega}U\overline{E}\nabla w_k d\Omega-i\overline{\widehat{k}}\delta\boldsymbol{x}_k\cdot\int_{\Gamma_{out}}U\overline{E}\nabla w_k d\Gamma\\
&\left.-2\pi c\varepsilon_0\frac{\kappa\eta}{\lambda}\left(\int_{\Omega^A}\overline{E}E\,\nabla w_k\,d\Omega-\int_{\Omega^A}w_k E\,\nabla\overline{E}d\Omega+\int_{\Omega^A}\overline{E}w_k\nabla Ed\Omega\right)\right\}.
\end{aligned}
\tag{42}
$$

The first four terms in Eq. (42) vanish because of the adjoint equation (33). Now we end up with

$$
\begin{aligned}
\delta\mathcal{L}(\delta\boldsymbol{x}_k)=&\Re\left\{-\delta\boldsymbol{x}_k\cdot\int_{\Omega}\nabla U\,\nabla w_k\cdot\nabla\overline{E}d\Omega-\delta\boldsymbol{x}_k\cdot\int_{\Omega}\nabla\overline{E}\nabla U\cdot\nabla w_k d\Omega\right.\\
&+\delta\boldsymbol{x}_k\cdot\int_{\Omega}\nabla w_k\nabla U\cdot\nabla\overline{E}d\Omega-\overline{\widehat{k}}^2\delta\boldsymbol{x}_k\cdot\int_{\Omega}\nabla w_k U\overline{E}d\Omega\\
&-i\overline{\widehat{k}}\delta\boldsymbol{x}_k\cdot\int_{\Gamma_{out}}U\overline{E}\nabla w_k d\Gamma\\
&\left.+2\pi c\varepsilon_0\frac{\kappa\eta}{\lambda}\delta\boldsymbol{x}_k\cdot\left(\int_{\Omega^A}\overline{E}E\nabla w_k d\Omega-\int_{\Omega^A}w_k E\nabla\overline{E}d\Omega+\int_{\Omega^A}\overline{E}w_k\nabla Ed\Omega\right)\right\}.
\end{aligned}
\tag{43}
$$

Therefore the gradient of the Lagrangian with respect to the design variation of mesh

nodes is

$$\frac{\partial \mathcal{L}}{\partial \boldsymbol{x}_k} = \frac{\delta \mathcal{L}}{\delta \boldsymbol{x}_k} = \Re \left\{ - \int_\Omega \nabla U \ \nabla w_k \cdot \nabla \overline{E} d\Omega - \int_\Omega \nabla \overline{E} \nabla U \cdot \nabla w_k d\Omega \right.$$
$$+ \int_\Omega \nabla w_k \nabla U \cdot \nabla \overline{E} d\Omega - \overline{\tilde{k}}^2 \int_\Omega \nabla w_k (U\overline{E}) d\Omega - i\overline{\tilde{k}} \int_{\Gamma_{out}} U\overline{E} \nabla w_k d\Gamma \qquad (44)$$
$$+ 2\pi c \varepsilon_0 \frac{\kappa \eta}{\lambda} \left(\int_{\Omega^A} \overline{E} E \nabla w_k d\Omega - \int_{\Omega^A} w_k E \ \nabla \overline{E} d\Omega + \int_{\Omega^A} \overline{E} w_k \nabla E d\Omega \right) \right\}.$$

Usually, Eq. (44) is evaluated by looping over all the finite elements, which could take significant amount of time when there is a large number of elements. Fortunately by making use of the weak form definition of PDEs in COMSOL, Eq. (44) can be assembled and extracted directly as the residual of a weak form equation defined on the same mesh used to solve the state and adjoint equations.

4.4   Mesh deformation

Since the shape will change during the optimization process, it is necessary to solve the equations on a new mesh corresponding to the deformed shape when using the finite element method. However, regenerating the mesh for each updated design is not only time consuming, but also will introduce noise in the objective function when adding or deleting mesh nodes. Moreover, we wish to establish a differentiable expression for the mesh node positions as a function of the design variables so that the nodal sensitivities, which are the sensitivities of the mesh node positions with respect to the design variables can be obtained analytically.

Noting that our initial computational domain is rectangular and the design boundaries are only deflected in the y- direction and assumed to be the same for all layer interfaces. Here we use a simple approach to deform the mesh from an initially generated mesh according to the design update. That is, all the mesh nodes are fixed in the x- direction and they are only moved in the y- direction by a distance which depends linearly on the design variables and their initial positions in the computation domain. According to our results of the numerical experiments, we clarify that the results obtained using such mesh deformation scheme are accurate and reliable as long as the maximum elements size does not exceed $1/20$ of the incident wavelength. Clearly if the interior layer interfaces are allowed to be different and large deformation occurs, re-meshing or a more elegant mesh deformation scheme such as elasticity based mesh movement will be preferred.

As shown in Fig. 3, the movements of the mesh nodes are calculated based on their initial positions in the domain. Let $\boldsymbol{x}_p$, $\boldsymbol{x}_q$, V_1 and V_2 be four nodes with same

$x-$ coordinates, while $\boldsymbol{x}_p$ and $\boldsymbol{x}_q$ are on the design shapes, V_1 and V_2 lie above and below the Air/ITO interface respectively. t_1 and t_2 are the thickness of the layers, d_1 and d_2 are the initial distance of node V_1 and V_2 from the incident boundary and design shape respectively. If the positions of $\boldsymbol{x}_p$ and $\boldsymbol{x}_q$ are moved by α_p and α_q, then the movements of V_1 and V_2 are calculated as

$$\begin{cases} \dfrac{d_1}{t_1} = \dfrac{d_1 + \delta y_1}{t_1 + \alpha_p}, \\ \dfrac{d_2}{t_2} = \dfrac{d_2 + \delta y_2 - \alpha_p}{t_2 + \alpha_q - \alpha_p}. \end{cases} \Rightarrow \begin{cases} \delta y_1 = \dfrac{d_1}{t_1}\alpha_p, \\ \delta y_2 = \alpha_p + \dfrac{d_2}{t_2}(\alpha_q - \alpha_p). \end{cases} \tag{45}$$
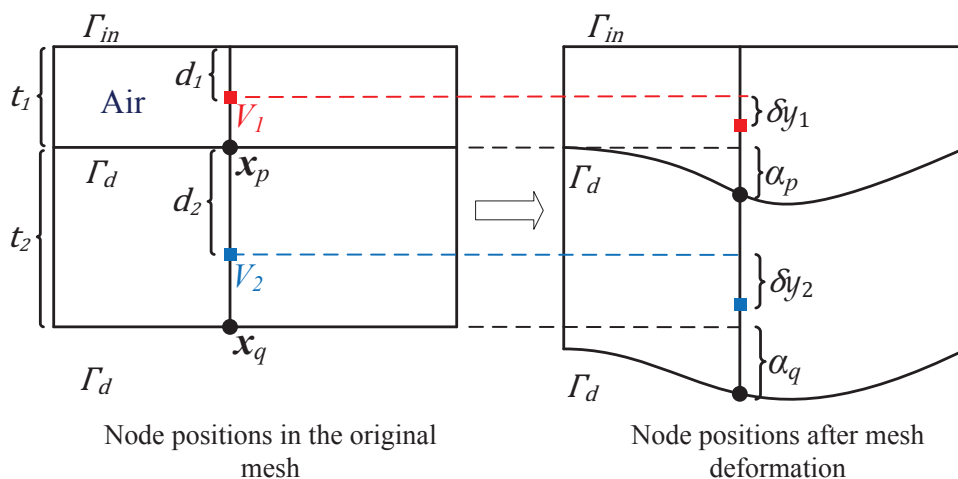
Figure 3: Illustration of mesh deformation.

This linear mapping can be written as

$$\delta \boldsymbol{x} = A\boldsymbol{\alpha}, \tag{46}$$

where $\delta \boldsymbol{x} = (\delta y_1, \delta y_2, \cdots, \delta y_N)^T$ is a column vector contains the position variations of each node, $\boldsymbol{\alpha}$ is a column vector contains all the n design variables, and A is a N by n matrix. Since A does not depend on the design variables, it can be pre-computed column by column by varying one design variable with unit change each time. The positions of mesh nodes are then updated as

$$\boldsymbol{x}_k = \boldsymbol{x}_k^0 + \delta \boldsymbol{x}_k, \tag{47}$$

where $\boldsymbol{x}_k^0$ is the initial position.

17

Now using Eq. (44) and (46), we can compute the sensitivity of the Lagrangian function with respect to the design variables as

$$\frac{\partial \mathcal{L}}{\partial \boldsymbol{\alpha}} = A^T \frac{\partial \mathcal{L}}{\partial \boldsymbol{x}}, \tag{48}$$

where

$$\frac{\partial \mathcal{L}}{\partial \boldsymbol{x}} = \left(\frac{\partial \mathcal{L}}{\partial \boldsymbol{x}_1}, \frac{\partial \mathcal{L}}{\partial \boldsymbol{x}_2}, \cdots, \frac{\partial \mathcal{L}}{\partial \boldsymbol{x}_N} \right)^T$$

.

5 Smoothing of design shapes

It is known that for shape optimization problem associated with elliptic boundary-value problems, such as the Helmholtz equation, the sensitivity of the objective function to oscillatory changes in the design may be low, which may cause the optimization to produce very oscillatory shapes [12]. In addition, when the positions of mesh nodes are used directly as the design variables, sharp corners are likely to appear in the design, which is not favourable in manufacturing. Therefore, approaches to suppress oscillations and sharp corners of the design shapes have to be developed.

For design shapes represented by B-splines, by choosing appropriate knot vectors and control points, sharp corners can be avoided and oscillations can also be controlled. For node based shape representation, we apply a Helmholtz PDE based filter on the variation of mesh nodes on the design boundary and compute a filtered field by solving the following Helmholtz equation,

$$
\begin{aligned}
-r^2 \tilde{\alpha}'' + \tilde{\alpha} &= \alpha, && \text{on } \Gamma_d^{ref}, \\
\tilde{\alpha} &= 0, && \text{at the end points on } \Gamma_d^{ref},
\end{aligned}
\tag{49}
$$

where α is the input design variable field, $\tilde{\alpha}$ is the filtered field and r is the length scale parameter. The effect of Helmholtz filter with different length parameters can be seen in Fig. 4. The black line is the unfiltered field, the red dashed line is the filtered field with the length parameter $r = 0.05$, the blue dotted line is the filtered field with the length parameter $r = 0.2$. As we can see the oscillation can be alleviated by increasing the length parameter. Eq. (49) is also solved using FEM on Γ_d^{ref} based on its discrete weak form

$$\int_{\Gamma_d^{ref}} (r^2 w_j'(\tilde{\alpha}^h)' + w_j(\tilde{\alpha}^h - \alpha^h)) d\Gamma = 0, \quad j = 1, 2, \cdots, n, \tag{50}$$

18
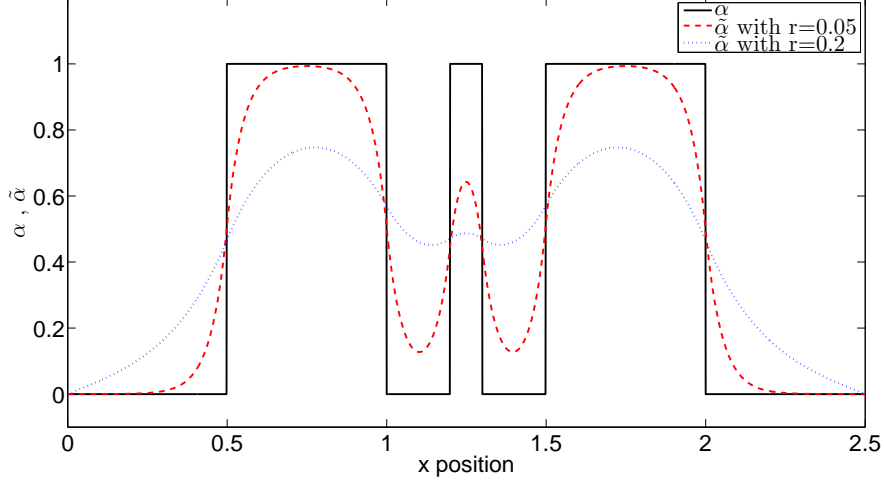
Figure 4: Effect of the Helmholtz filter with different length parameters.

where $w_j(\boldsymbol{x})$ is the standard 1D basis function and n is the number of nodes on Γ_d^{ref}. In matrix form Eq. (50) can be written as

$$\boldsymbol{K}\tilde{\boldsymbol{\alpha}} = \boldsymbol{M}\boldsymbol{\alpha}, \tag{51}$$

where $\tilde{\boldsymbol{\alpha}} = (\tilde{\alpha}_1, \tilde{\alpha}_2, \cdots, \tilde{\alpha}_n)^T$, $\boldsymbol{\alpha} = (\alpha_1, \alpha_2, \cdots, \alpha_n)^T$, $K_{jk} = \int_{\Gamma_d^{ref}} (r^2 w_j' w_k' + w_j w_k) d\Gamma$ and $M_{jk} = \int_{\Gamma_d^{ref}} w_j w_k d\Gamma$. The filtered gradient can be derived in the same form as the filtered variables.

$$\boldsymbol{K}\frac{\partial \mathcal{L}}{\partial \tilde{\boldsymbol{\alpha}}} = \boldsymbol{M}\frac{\partial \mathcal{L}}{\partial \boldsymbol{\alpha}} \tag{52}$$

6   Numerical results

In this section we report numerical results of shape optimization for a bulk heterojunction OSC using the presented approach. The simulated OSC consists of four layers from top to bottom are ITO (100 nm), PEDOT:PSS (50 nm), P3HT:PCBM (thickness can be varied) and Al (250 nm) respectively with thickness indicated in the parenthesis. An air layer with thickness of 200 nm is also included in the model from which the light travels through and incidents on the OSC. The width of the structure is set as 3000 nm. The complex refraction indices $\tilde{n}$ of the materials are obtained from the literature [31, 32, 33, 34]. For the incident light unless otherwise specified we choose wavelength range of $350 - 800$ nm of the AM 1.5G sunlight spectrum

[7]. The finite element analysis is implemented in COMSOL with Matlab Livelink. Specifically, we use COMSOL to solve Eq. (12) and assemble the sensitivity gradient (44) through Matlab script. The optimization is done using the method of moving asymptotes (MMA) [29]. Since MMA solves an approximated problem in each iteration, the process tends to oscillate sometimes. In this case a move limit δ will be imposed to restrict the change of design variables between iterations and make the approximation of the original problem more conservative. The convergence criteria used is the change of objective function values, i.e. $\varepsilon = \left| \dfrac{f^{(k)} - f^{(k-1)}}{f^{(0)}} \right| \leq 10^{-5}$ where $f^{(k)}$ is the objective function value at the $k-$th iteration. The numerical experiments presented in this section were performed on a desktop computer with Intel® Core™ i7-2600K Processor (8M Cache, 3.4 GHz).

6.1   Mesh convergence

Quadrilateral linear meshes are used throughout the optimization. To balance accuracy and efficiency the mesh is constructed such that it is very fine near the interfaces between layers and relatively coarse elsewhere. Three finite element meshes with different resolution are used to discretize the domain. The first mesh has 7500 elements with initial maximum element size of 30 nm, as shown in Fig. 5, the second and third mesh has initial maximum element size of 20 nm and 10 nm respectively. These meshes are tested for an incident wavelength of 550 nm. The mesh of the optimized shape is shown in Fig. 6, though there is some distortion, the mesh is still valid. In Fig. 7, we can see the optimized shapes are almost the same when the resolution is increased. The zoom-in view in Fig. 7(b) shows that using the first mesh results in the loss of some small features in the design because of the relative large element size. Therefore for all the following results we choose the mesh with initial maximum element size of 20 nm throughout the optimization and use the planar structure as the initial design.

(a) Quadrilateral linear mesh with maximum element size of 20 nm. Different colours are shown for different layers.

(b) Thickness of each layer.

Air (200 nm)
ITO (100 nm)
PEDOT:PSS (50 nm)
P3HT:PCBM (75 nm)
Al (250 nm)
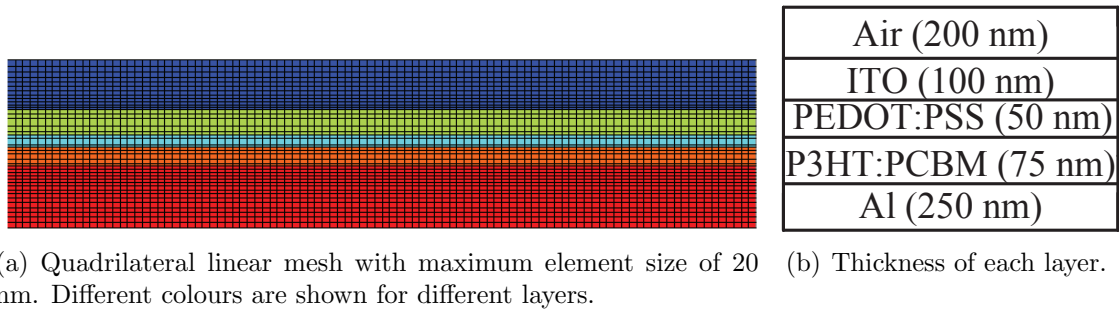
Figure 5: Simulated OSC structure.

(a) Mesh of optimized shape of the whole structure.

(b) Zoom in view.
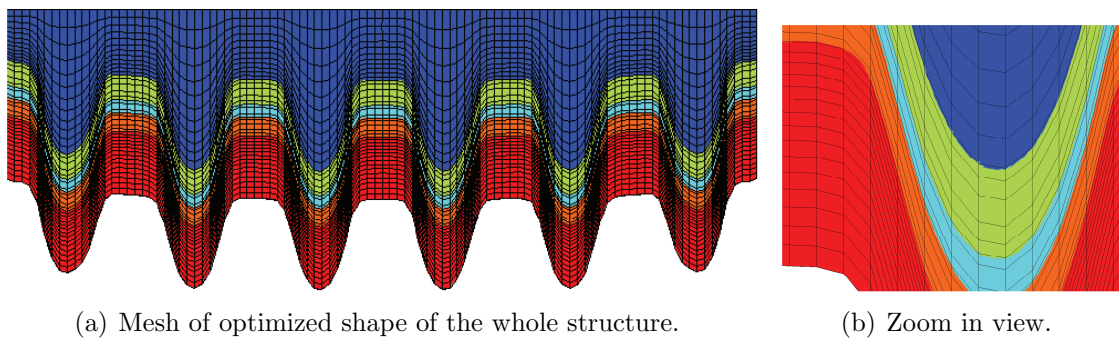
Figure 6: Mesh of optimized shape.

(a) Mesh of the entire domain.

(b) Zoom-in view of (a).
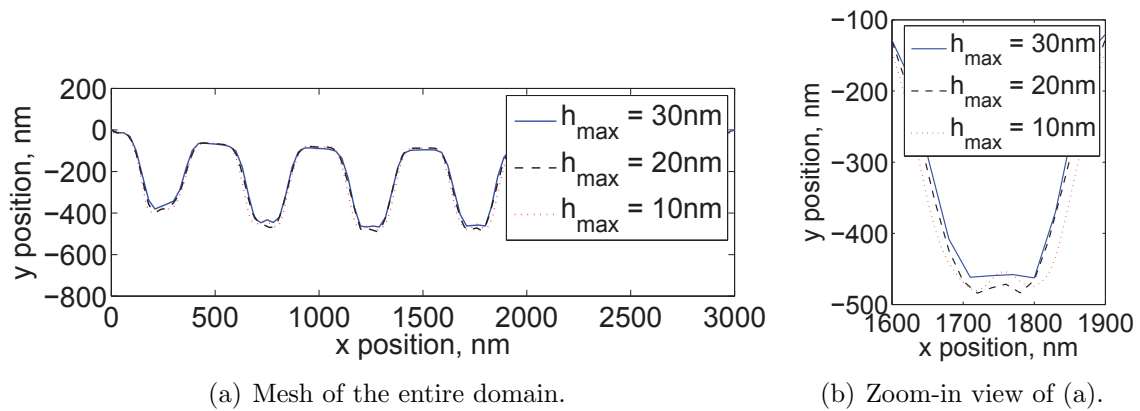
Figure 7: Optimized shapes for wavelength of 550 nm with three different meshes in Fig. 5. The filter radius of the Helmholtz filter is $r = 40$.

6.2 Design of V-shaped structure

To verify our approach, we optimized an OSC structure described in [9], where Nalwa et al proposed a V-shaped structure (Fig. 8(a)) with opening (7/10th of pitch) and bottom width (1/10th of pitch) fixed for a given pitch size. They demonstrated that for a given pitch size of 2 μm, the optimal pitch-height ratio for this structure was 4 : 3.

In our optimization, while using the two different boundary representations in Fig. 2, we constrain the design boundary to be the V-shape by setting the nodes or control points on the two sides of the V-groove to be on the same line. The horizontal positions of the nodes or control points are fixed, leaving only one design variable, the height, for the optimization. The range of wavelengths chosen for the simulations is $300 - 700$ nm with incident power being defined by AM 1.5 sun light spectra. Same materials as in [9] are used for each layer in the OSC and the light absorption in the active layer is used as the cost function. The optimal pitch-height ratio is 4 : 2.9 from our optimization which is very close to the value 4 : 3 as reported in [9]. The difference could be attributed to that, in [9], the area of the active layer changes with the overall structure height, while in our method the area is kept constant during the optimization. The advantage of our approach is that it takes much less time to find the optimal structure using gradient based search algorithm than sweeping a wide range of parameters.

6.3 Optimization results for single wavelength incident light

To find the optimal shape with maximum light absorption, the formulation in Eq. (20) is used. First we optimize the OSC shape with incident light of single wavelength $\lambda = 550$ nm. The layers of the simulated OSC from top to bottom are Air (200 nm), ITO (100 nm), PEDOT:PSS (50 nm), P3HT:PCBM (75 nm) and Al (250 nm) respectively with thickness indicated in the parenthesis.

During the optimization process we observed that, when using the node based shape representation method presented in Section 3, if no filters were applied, the optimization produced irregular shapes with very sharp corners as shown in Fig. 9. The figure also shows the results are mesh dependent as the oscillation increases for finer mesh. After applying the Helmholtz filter the sharp corners are smoothed out. On the other hand, if we choose B-spline to represent the design shape, its curvature can be adjusted by setting the distance between control points. Fig. 10 shows the optimized shape for wavelength of 550 nm using Helmholtz filter and B-spline curves respectively with different length scales. As we can see, the figures in each row have the similar shape with close objective values using the two different
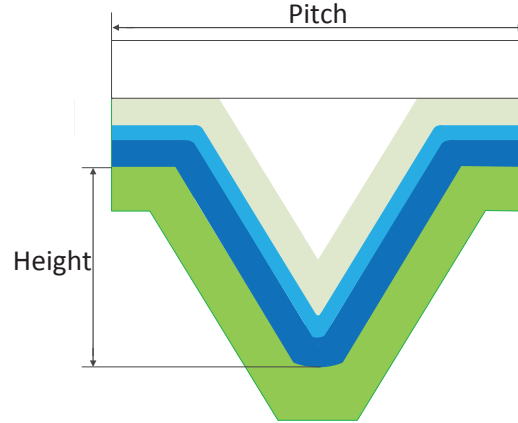
(a) Schematic representation of an OSC with V-shaped pitch structure [9].
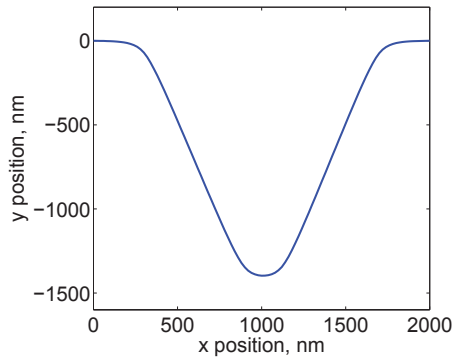
(b) Optimized shape with node based shape representation. A filter radius of $r = 60$ is used. The optimal pitch-height ratio is $4 : 2.9$.
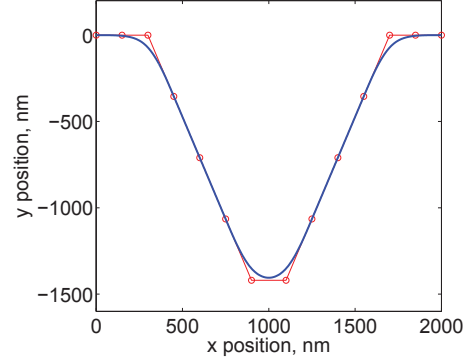
(c) Optimized shape with B-spline shape representation. The optimal pitch-height ratio is $4 : 2.9$.

Figure 8: Optimized results for V-shaped OSC.

methods. Also, column-wise, increasing the filter size and distance between control points have the same effect making the shape smoother. In addition, Using B-spline representation allows us to use much fewer design variables than using the node based representation which depends on mesh resolution. Usually fewer design variables leads to less optimization time, as shown in Fig. 11 where the convergence history for results obtained in Fig. 10(e) and 10(f) is presented. Table 1 also lists the detail data of the optimizations in Fig. 11. The optimization converges in less than 40 iterations when using B-spline based representation. When using node based

23

Table 1: Data of optimization using node based representation and B-spline based representation for $\lambda = 550$ nm. The optimized shapes are shown in Fig. 10(e) and 10(f).

Shape representation	No. of design variables	No. of Iteration	Time(min)	$\dfrac{\mathcal{F}_{opt}}{\mathcal{F}_0}$
Node based	149	97	12.5	1.388
B-spline based	29	32	4.3	1.376

representation, convergence is obtained in nearly 100 iterations.

(a) Initial maximum element size is 20 nm. (b) Initial maximum element size is 5 nm.
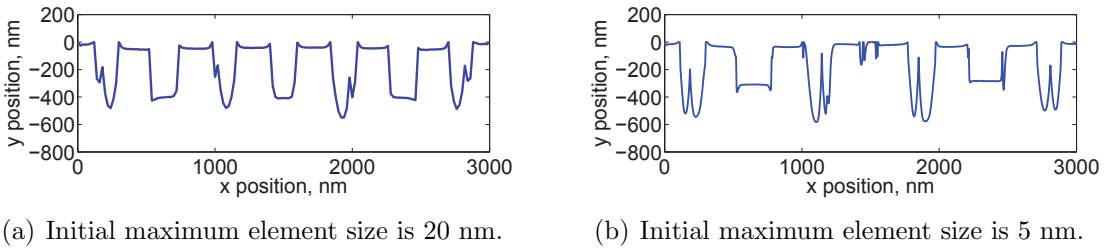
Figure 9: Optimized shape using node based representation without Helmholtz filter, for incident light with wavelength $\lambda = 550$ nm. The results are shown to be mesh dependent as the oscillation increases for finer mesh.

Another important observation of our optimization is that all the optimized shapes show periodicity, which confirms the grating effect of the textured structure [35]. Fig. 12 shows the distribution of the light absorption in the structure before and after optimization for different wavelengths. As can be seen, the light absorption has been amplified significantly in the active layer (75 nm thickness) in the optimized structure.

6.4   Optimization results for multi-wavelength incident light

In practice the incident light for OSCs is usually the sunlight. Here we choose the wavelength range of $350 - 800$ nm based on the absorption spectrum of the material. To save computation time, the incident light is simulated from $350 - 800$ nm with a step size of 10 nm, which gives the very close result (with relative error of 10^{-4}) compared with step size of 1 nm. The thickness of the active layer of OSC is fixed at 75 nm. The length parameter r of the Helmholtz filter and the distance Δx between control points are chosen based on the results shown in Fig. 10 so that

24

(a) $r = 60$ nm, $\delta = 3$, $\mathcal{F}_{opt}/\mathcal{F}_0 = 1.402$

(b) $\Delta x = 60$ nm, $\delta = 5$, $\mathcal{F}_{opt}/\mathcal{F}_0 = 1.401$

(c) $r = 100$ nm, $\delta = 10$, $\mathcal{F}_{opt}/\mathcal{F}_0 = 1.392$

(d) $\Delta x = 75$ nm, $\delta = 10$, $\mathcal{F}_{opt}/\mathcal{F}_0 = 1.381$

(e) $r = 120$ nm, $\delta = 8$, $\mathcal{F}_{opt}/\mathcal{F}_0 = 1.388$

(f) $\Delta x = 100$ nm, $\delta = 10$, $\mathcal{F}_{opt}/\mathcal{F}_0 = 1.376$
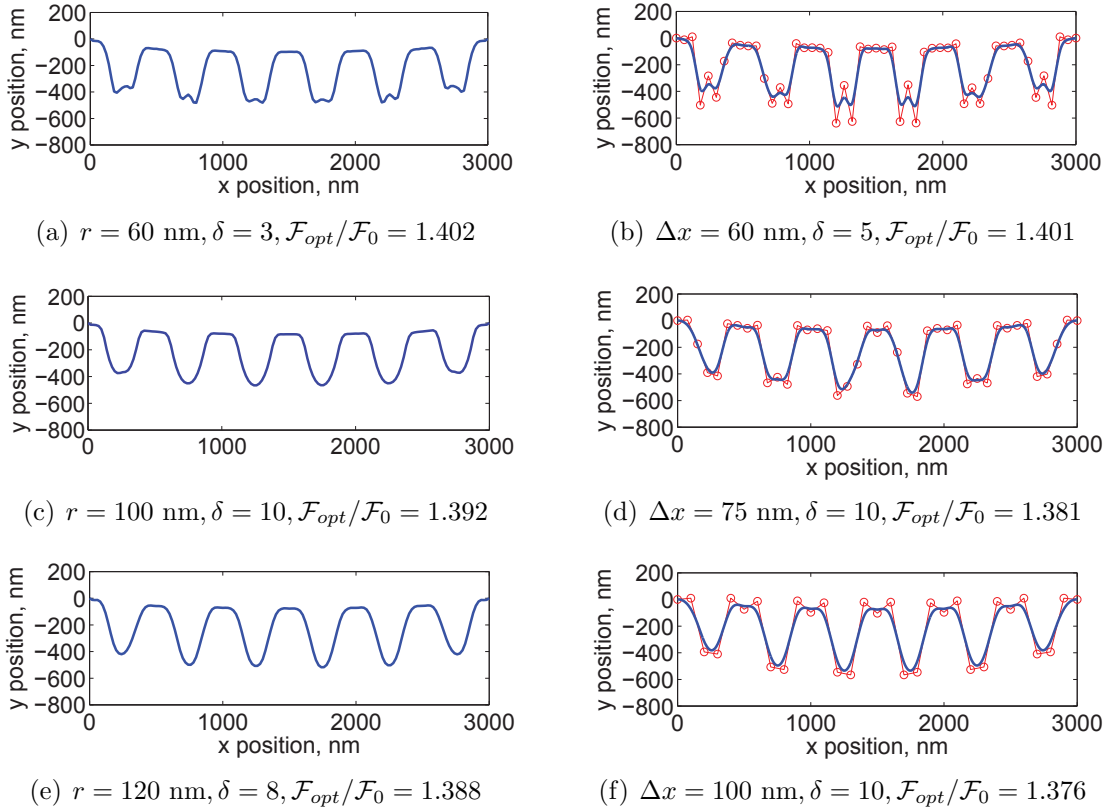
Figure 10: Comparison of results using Helmholtz filter (left column) and B-splines (right column) for incident light with wavelength $\lambda = 550$ nm. $\mathcal{F}_0$ and $\mathcal{F}_{opt}$ are the objective values of initial planar and optimized structures respectively, r is the Helmholtz filter radius, δ is the move limit of the MMA algorithm and Δx is the distance between adjacent control points. The number of design variables is 149 for the left column, and 99, 49, 39, 29 respectively for the right column (from top to bottom).

the optimized shape is smooth enough. From the result in Fig. 13, we can see that the periodicity still exists even for multi-wavelength incident light, with the peak distance approximately 300 nm and height 120 nm.

To further explore the potential improvement of light absorption with optimized shape, we conduct another optimization starting from an initial planar structure where the active layer thickness has already been optimized. In [36], Liu et al calculated the light absorption in the active layer with different thickness and showed
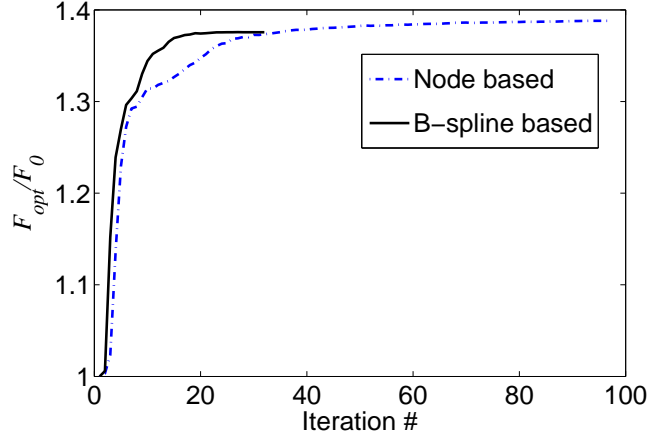
Figure 11: Convergence history for node based shape representation and B-spline based shape representation.

that the optimal thickness is around 87 nm in the range of $0 - 150$ nm.. We start the optimization with this initial design and set the maximum active layer thickness as 150 nm since the charger collection is efficient within this limit [36]. The optimized shape is shown in Fig. 14 with the optimized active layer thickness of 150 nm. An improvement of 27% over the initial design is observed. We also observe that the optimal active layer thickness increases as we increase the thickness limit. This indicates an important advantage of such grating based structure, that is in textured structure the optimal active layer thickness could be much larger than in planar structure. This is because in planar structures increasing active layer thickness sometimes even results in poor electric field distribution and light absorption [36, 37], which do not exist in textured structures due to the grating effect [35].

(a) $\lambda = 500$ nm, initial structure   (b) $\lambda = 500$ nm, optimized structure

(c) $\lambda = 550$ nm, initial structure   (d) $\lambda = 550$ nm, optimized structure

(e) $\lambda = 600$ nm, initial structure   (f) $\lambda = 600$ nm, optimized structure
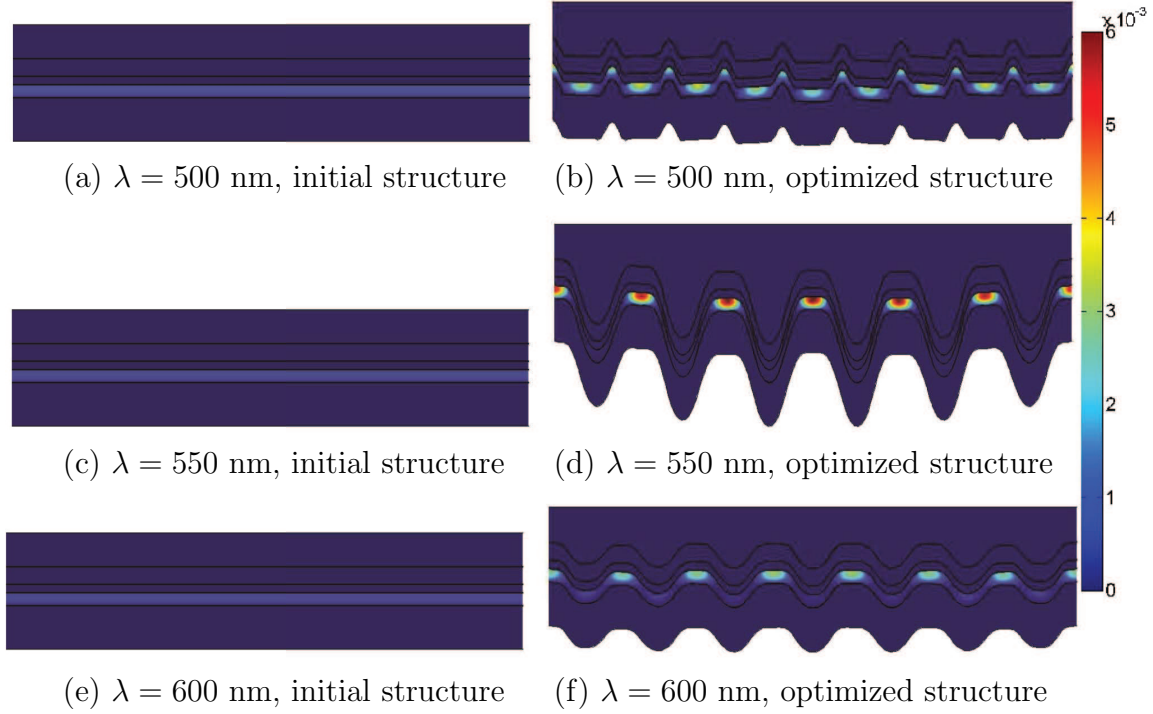
Figure 12: Distribution of light absorption in the OSC before and after optimization for different wavelengths. The black lines indicate the interior boundaries of different layers.

(a) $r = 100$ nm, $\mathcal{F}_{opt}/\mathcal{F}_0 = 1.146$ (b) $\Delta x = 100$ nm, $\mathcal{F}_{opt}/\mathcal{F}_0 = 1.142$
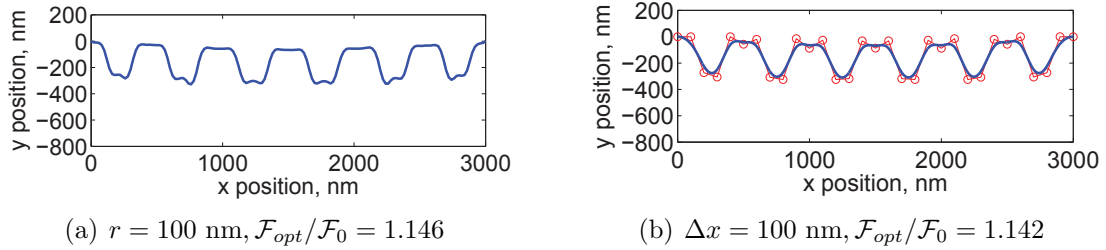
Figure 13: Optimized shapes for multi-wavelength of $350-800$ nm using different representations for the design shape (left: node based representation where Helmholtz filter is applied; right: B-spline representation).

(a) $r = 100$ nm, $\mathcal{F}_{opt}/\mathcal{F}_0 = 1.27$ (b) $\Delta x = 100$ nm, $\mathcal{F}_{opt}/\mathcal{F}_0 = 1.28$
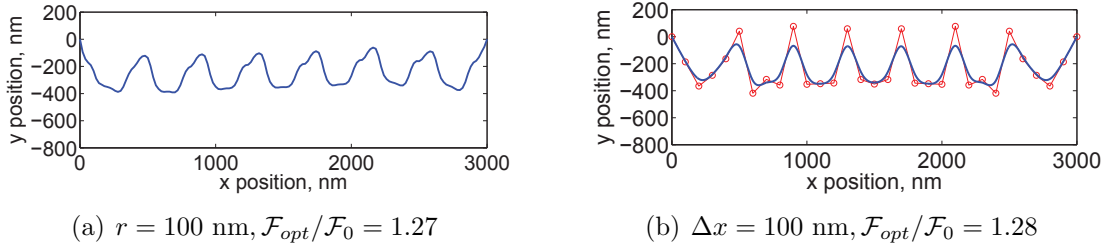
Figure 14: Optimized shapes for OSC with initial active layer thickness of 87 nm (left: node based representation where Helmholtz filter is applied; right: B-spline representation). The optimized thickness of active layer is 150 nm.

7 Conclusion

This paper presents a method for gradient based shape optimization for organic thin film solar cells based on the optical modeling. The analytical sensitivity is derived using discrete adjoint method and computed efficiently. The periodic structures are observed for all the optimized shapes. Comparing with planar structure with optimal thickness of active layer, a further increase of about 27% in light absorption can be achieved in the active layer with thickness of 150 nm. Another interesting observation is that, for all wavelength incident light, the groove in the optimized shape is very low (around 100 nm) and not difficult to fabricate, which makes it very promising.

Particularly, using the Maxwell equations to describe light propagation in structures allow us to model arbitrary shaped OSCs. The optimization can start with any initial geometry without the need of selecting a priori shape, and leads to the true optimal shape of the problem.

We also compare the results of using node based shape representations with Helmholtz filter and B-splines to control the smoothness of the design shapes. The two approaches are shown to have similar effect on smoothing the design shapes. However, there are fewer design variables which are independent of mesh resolution when using B-splines to represent the design shapes, leading to fewer iterations and less optimization time. It is also compatible with and can be used directly in CAD and blueprint.

Our method can be directly applied on other kinds of solar cells, such as Si based and polymer tandem cells. Thickness optimization can also be done by constraining the movement of design variables. Future work will include optimization for the overall performance of OSCs based on coupled optical and electrical models and an extension to the 3D case.

References

[1] S.E. Shaheen, D.S. Ginley, and G.E. Jabbour. Organic-based photovoltaics: toward low-cost power generation. *MRS bulletin*, 30(01):10–19, 2005.

[2] C. Deibel and V. Dyakonov. Polymer–fullerene bulk heterojunction solar cells. *Reports on Progress in Physics*, 73(9):096401, 2010.

[3] A. Raman, Z. Yu, and S. Fan. Dielectric nanostructures for broadband light trapping in organic solar cells. In *CLEO: Science and Innovations*. Optical Society of America, 2011.

[4] S.B. Mallick, N.P. Sergeant, M. Agrawal, J.Y. Lee, and P. Peumans. Coherent light trapping in thin-film photovoltaics. *MRS BULLETIN*, 36, 2011.

[5] L. Liu and G. Li. Investigation of recombination loss in organic solar cells by simulating intensity-dependent current-voltage measurements. *Solar Energy Materials and Solar Cells*, 2011.

[6] C. Deibel, A. Wagenpfahl, and V. Dyakonov. Influence of charge carrier mobility on the performance of organic solar cells. *physica status solidi (RRL)–Rapid Research Letters*, 2(4):175–177, 2008.

[7] G. Li, L. Liu, F. Wei, S. Xia, and X. Qian. Recent progress in modeling, simulation, and optimization of polymer solar cells. *Photovoltaics, IEEE Journal of*, 2(3):320 –340, July 2012.

[8] S. Yu, C. Wang, C. Sun, and W. Chen. Topology optimization for highly-efficient light-trapping structure in solar cell. *10th World Congress on Structural and Multidisciplinary Optimization*, Orlando, U.S.A, May 2013.

[9] K.S. Nalwa and S. Chaudhary. Design of light-trapping microscale-textured surfaces for efficient organic solar cells. *Optics Express*, 18(5):5168–5178, 2010.

[10] K. Tvingstedt, S. Dal Zilio, O. Inganäs, and M. Tormen. Trapping light with micro lenses in thin film organic photovoltaic cells. *Optics Express*, 16(26):21608–21615, 2008.

[11] Dorin Bucur. How to prove existence in shape optimization. *Control and Cybernetics*, 34(1), 2005.

[12] O. Pironneau. *Optimal shape design for elliptic systems*. Springer-Verlag, 1984.

[13] M. Hinze, R. Pinnau, M. Ulbrich, and S. Ulbrich. *Optimization with PDE constraints*, volume 23. Springer, 2008.

[14] B.J. Geurts, A.K. Kuczaj, and E.S. Titi. Regularization modeling for large-eddy simulation of homogeneous isotropic decaying turbulence. *Journal of Physics A: Mathematical and Theoretical*, 41:344008, 2008.

[15] B.S. Lazarov and O. Sigmund. Filters in topology optimization based on Helmholtz-type differential equations. *International Journal for Numerical Methods in Engineering*, 86(6):765–781, 2011.

[16] X. Qian and O. Sigmund. Topological design of electromechanical actuators with robustness toward over- and under-etching. *Computer Methods in Applied Mechanics and Engineering*, 253(0):237 – 251, 2013.

[17] J.I. Toivanen, R.A.E. Mäkinen, J. Rahola, S. Järvenpää, and P. Ylä-Oijala. Gradient-based shape optimisation of ultra-wideband antennas parameterised using splines. *Microwaves, Antennas & Propagation, IET*, 4(9):1406–1414, 2010.

[18] X. Qian and O. Sigmund. Isogeometric shape optimization of photonic crystals via Coons patches. *Computer Methods in Applied Mechanics and Engineering*, 200(25):2237–2255, 2011.

[19] X. Zhu, W.C.H. Choy, F. Xie, C. Duan, C. Wang, W. He, F. Huang, and Y. Cao. A study of optical properties enhancement in low-bandgap polymer solar cells with embedded PEDOT: PSS gratings. *Solar Energy Materials and Solar Cells*, 2012.

[20] K.Y. Suh and H.H. Lee. Capillary force lithography: large-area patterning, self-organization, and anisotropic dewetting. *Advanced Functional Materials*, 12(6-7):405–413, 2002.

[21] Kanwar S Nalwa, Joong-Mok Park, Kai-Ming Ho, and Sumit Chaudhary. On realizing higher efficiency polymer solar cells using a textured substrate platform. *Advanced Materials*, 23(1):112–116, 2011.

[22] S.I. Na, S.S. Kim, S.S. Kwon, J. Jo, J. Kim, T. Lee, and D.Y. Kim. Surface relief gratings on poly (3-hexylthiophene) and fullerene blends for efficient organic solar cells. *Applied Physics Letters*, 91(17):173509–173509, 2007.

[23] S.H. Park, A. Roy, S. Beaupré, S. Cho, N. Coates, J.S. Moon, D. Moses, M. Leclerc, K. Lee, and A.J. Heeger. Bulk heterojunction solar cells with internal quantum efficiency approaching 100%. *Nature Photonics*, 3(5):297–302, 2009.

[24] V. Andersson, K. Tvingstedt, and O. Inganäs. Optical modeling of a folded organic solar cell. *Journal of Applied Physics*, 103:094520, 2008.

[25] J. Jin. *Finite element method in electromagnetics*. John Wiley, 2002.

[26] Arnold Sommerfeld. *Partial differential equations in physics*, volume 1. Academic Press, New York, 1949.

[27] David L Colton and Rainer Kress. *Integral equation methods in scattering theory*, volume 57. Wiley New York, 1983.

[28] Y He and BZ Guo. The existence of optimal solution for a shape optimization problem on starlike domain. *Journal of Optimization Theory and Applications*, 152(1):21–30, 2012.

[29] K. Svanberg. The method of moving asymptotes—a new method for structural optimization. *International Journal for Numerical Methods in Engineering*, 24(2):359–373, 2005.

[30] Michael C Delfour and Jean-Paul Zolésio. *Shapes and geometries: metrics, analysis, differential calculus, and optimization*, volume 22. Siam, 2011.

[31] E. Lioudakis, A. Othonos, I. Alexandrou, and Y. Hayashi. Optical properties of conjugated poly(3-hexylthiophene)/[6, 6]-phenylC_{61}-butyric acid methyl ester composites. *Journal of Applied Physics*, 102(8):083104–083104, 2007.

[32] L.A.A. Pettersson, F. Carlsson, O. Inganäs, and H. Arwin. Spectroscopic ellipsometry studies of the optical properties of doped poly (3, 4-ethylenedioxythiophene): an anisotropic metal. *Thin Solid Films*, 313:356–361, 1998.

[33] J. Bartella, J. Schroeder, and K. Witting. Characterization of ITO-and TiO_xN_y films by spectroscopic ellipsometry, spectraphotometry and XPS. *Applied Surface Science*, 179(1):181–190, 2001.

[34] P.B. Johnson and R.W. Christy. Optical constants of transition metals: Ti, V, Cr, Mn, Fe, Co, Ni, and Pd. *Physical Review B*, 9(12):5056, 1974.

[35] C.A. Palmer and E.G. Loewen. *Diffraction grating handbook*. Richardson Grating Laboratory, 2000.

[36] L. Liu and G. Li. Thickness optimization of organic solar cells by optical transfer matrix. In *Nanotechnology (IEEE-NANO), 2011 11th IEEE Conference on*, pages 332–336. IEEE, 2011.

[37] G. Dennler, M.C. Scharber, and C.J. Brabec. Polymer-fullerene bulk-heterojunction solar cells. *Advanced Materials*, 21(13):1323–1338, 2009.